Analysis and modeling of PEMFC degradation: Effect on oxygen transport

Shinji Jomori*, Nobuaki Nonoyama, Toshihiko Yoshida

Fuel Cell System Development Div. Toyota Motor Corporation, 1200 Mishuku, Susono, Shizuoka 410-1193, Japan

HIGHLIGHTS

► This article quantifies and models the impact of catalyst layer area loss during operation on fuel-cell performance.
► Oxygen transport through the ionomer film is shown to become limiting due to the reduced area for reaction.
► Both modeling and experiments are undergone.

ARTICLE INFO

ABSTRACT

During proton-exchange-membrane-fuel-cell degradation various changes occur in the membrane-electrode assembly, and consequently the performance decays. Therefore, the correlation between physical property changes and the performance decay is important. In this paper, we focus on this correlation and have developed a quantitative model to estimate the performance decay after degradation. Comparison of electrochemical surface area (ECSA) and polarization curves before and after potential cycling demonstrates that there was more performance decay than that estimated due only to ECSA decrease, especially at higher current densities. This large performance decay is estimated and quantitatively simulated to be due to the increase in oxygen transport resistance caused by the oxygen transport through the ionomer film coating the Pt/C particles in the cathode catalyst layer. It is shown that the data can be fit by assuming that the effective ionomer film area is proportional to ECSA. According to our results, the transport resistance increased significantly during potential cycling and more than half of the performance decay at high current densities originated from the increased transport overpotential. The effect of proton overpotential in the cathode catalyst layer was also studied with additional performance decay witnessed under low-humidity conditions.

© 2012 Elsevier B.V. All rights reserved.

1. Introduction

Proton-exchange-membrane fuel cells (PEMFCs) are one of the strongest candidates for future automobile applications due to their high efficiency and clean emissions. In automobile applications, a PEMFC must be designed not only to work under a wide range of conditions but also to maintain its performance for long-term use over years. Therefore, understanding and optimizing the degradation mechanisms is critical throughout the entire lifespan of the cell; modeling is ideally suited to examine these tradeoffs. Here, 'degradation' includes both physical property changes and performance decay. Typical physical property changes observed in PEMFCs include decreasing electrochemical surface area (ECSA) by dissolution of Pt, carbon corrosion, thinning of the catalyst layer

and membrane, sintering of Pt particles, etc., while performance decay means the decline of the polarization curve performance due to the above physical property changes. There have been plenty of papers published recently concerning property and phenomenological changes during degradation [1–13], however, the correlation between these physical properties changes and performance decay has not been fully explained.

Among various physical property changes, ECSA decrease by Pt dissolution is one of the main phenomena. Assuming only a decline in activity, the cell voltage should drop by the same degree over the entire current-density range due to ECSA decrease based on the Tafel equation

$$\eta_{ORR} = \frac{RT}{\alpha_C F} \ln \left(\frac{i_{ORR}}{A_{Pt} i_{0,ORR}^{ref}} \right) \tag{1}$$

where η_{ORR} is the activation overpotential, R is the ideal-gas constant, T is the absolute temperature, F is Faraday's constant,

* Corresponding author. Tel.: +81 55 997 7843; fax: +81 55 997 7120.
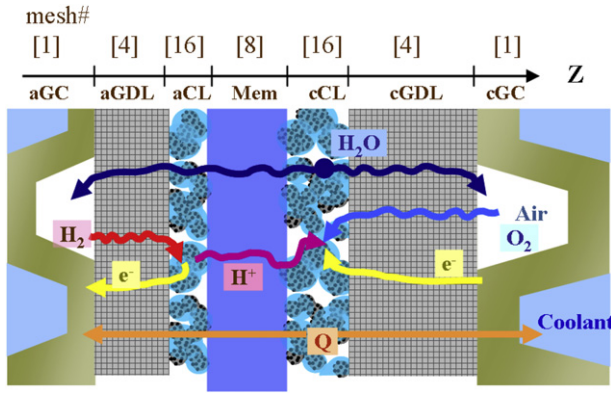E-mail address: shinji@jomori.tec.toyota.co.jp (S. Jomori).

Fig. 1. Schematic illustration of the one-dimensional PEMFC model.

$A_{\text{Pti0ref,ORR}}$ is the effective exchange current density, α_c is the cathodic transfer coefficient, and i_{ORR} is the reaction current density. However, significant performance decay in the high-current-density range is often observed in experiments that deviate from the expected decline given by the Tafel equation [11–13]. Some reports attribute this to ionomer degradation [14], but a quantitative analysis has not been conducted.

In our recent study [15,16], the oxygen transport resistance of a PEMFC was quantified by measuring the limiting current density using diluted oxygen by N_2 or He. We found that the oxygen permeation through the ionomer film is a major portion of the total transport resistance through the cathode catalyst layer, especially for low-Pt-loaded catalyst layers. This effect has also been shown in various modeling studies to be a critical issue [17,18]. Therefore, we anticipate that the performance decay might have a similar effect with the oxygen transport resistance.

The aim of this study is to analyze quantitatively the performance decay and develop an estimation technique of polarization curves after degradation, especially at high current densities, because such a technique has not been effectively established yet. To analyze the mechanism, we use both experiments and a 1D mathematical simulation with a detailed catalyst-layer model to evaluate the measure polarization curve. Furthermore, we simulate the impact of different operating conditions on the performance after degradation such as under low humidity and low oxygen to ascertain their effects.

2. Modeling

2.1. One-dimensional cell model

The one-dimensional model of each component of the PEMFC (see Fig. 1), i.e. gas-diffusion layer (GDL) and membrane-electrode-assembly (MEA) composed of catalyst layers (CLs) and membrane (Mem), was constructed with general physical equations (mass balance, heat balance, reactions, etc.) [19]. The five-layer 1D model includes about 80 physical properties of the various cell components. The governing equations of each PEMFC component are summarized in Table 1. Additional kinetic and physical-property equations are listed in Table 2. Based on these equations, the 1D model of each component of PEMFC was constructed using a commercial process modeling software, gPROMS® [20]. The components were connected to each other by defining continuity of all variables. The other model parameters, physical properties, are in Table 3. These models are developed with the following assumptions:

a. Ideal gas
b. No liquid water in the cell; excess water exists as supersaturated vapor or mist.

Table 1
Governing equations for steady state calculation.

	GDL	CL	Mem
Energy balance	$0 = \nabla\cdot(k_q\nabla T) + Q$ $Q = i^2/\sigma_e$	$0 = \nabla\cdot(k_q\nabla T) + Q$ (anode)$Q = i_{\text{HOR}}\eta_{\text{HOR}} + (FN_{H^+})^2/\kappa_M^{\text{eff}} + i^2/\sigma_e + 42000J_{\text{GM}}$ (cathode)$Q = i_{\text{ORR}}(\eta_{\text{ORR}} + 0.25) + (FN_{H^+})^2/\kappa_M^{\text{eff}} + i^2/\sigma_e + 42000J_{\text{GM}}$	$0 = \nabla\cdot(k_q\nabla T) + Q$ $Q = (FN_{H^+})^2/\kappa_M$
Mass balance (gas phase)	$v_G = -k_G/\mu\nabla P$ $0 = \nabla\cdot N_i$ $\nabla C_i = \sum_j \left(C_iJ_i - C_jJ_i/C_{\text{total}}D_{i,j}^{\text{eff}}\right)$ $N_i = J_i + C_iv_G$	$v_G = -k_G/\mu\nabla P$ (anode)$0 = \nabla\cdot N_{H_2} + i_{\text{HOR}}/2F$ (cathode)$0 = \nabla\cdot N_{O_2} + i_{\text{ORR}}/4F$ $0 = \nabla\cdot N_{N_2}$ $0 = \nabla\cdot N_{\text{vap}} + J_{\text{GM}}$ $J_i = D_{\text{Kund},i}^{\text{eff}}\nabla C_i$ $N_i = J_i + C_iv_G$	$N_i = \Psi_i\nabla P_i$ $0 = \nabla\cdot N_i$ (Crossover gas)
(ionomer phase)	-	$0 = -\nabla\cdot N_{\text{wat,M}} + J_{\text{GM}}$ $N_{\text{wat,M}} = \xi N_{H^+} - D_{\text{wat}}^{\text{eff}}\nabla C_{\text{wat,M}}$	$0 = \nabla\cdot N_{\text{wat,M}}$ $N_{\text{wat,M}} = \xi N_{H^+} - D_{\text{wat}}\nabla C_{\text{wat,M}}$
(Phase change flux)	-	$J_{\text{GM}} = k_{\text{GM}}(C_{\text{vap}} - C_{\text{vap}}^{\text{eq}})$	-
Charge balance (carbon phase)	$0 = \nabla\cdot(\sigma_e\nabla\Phi_C)$	(anode)$0 = \nabla\cdot(\sigma_e\nabla\Phi_C) - i_{\text{HOR}}$ (cathode)$0 = \nabla\cdot(\sigma_e\nabla\Phi_C) + i_{\text{ORR}}$	-
(ionomer phase)	–	(anode)$0 = \nabla\cdot(FN_{H^+}) + i_{\text{HOR}}$ (cathode)$0 = \nabla\cdot(FN_{H^+}) - i_{\text{ORR}}$ $FN_{H^+} = -\kappa_M^{\text{eff}}\nabla\Phi_M$	$0 = \nabla\cdot N_{H^+}$ $FN_{H^+} = -\kappa_M\nabla\Phi_M - \dfrac{\kappa_M\xi\nabla\mu_W}{F}$

Table 2
Kinetic equations and physical property calculation.

HOR kinetic equations
$$i_{HOR} = A_{Pt}i_0 \left(\frac{P_{H_2}}{P_{H_2}^{ref}} \exp\left(\frac{\alpha_a F}{RT}\eta_{HOR}\right) - \exp\left(\frac{-\alpha_c F}{RT}\eta_{HOR}\right) \right) \quad [Am^{-3}]$$

HOR overpotential
$$\eta_{HOR} = -\Phi_C + \Phi_M - U_{HOR} \quad [V]$$

HOR equilibrium potential
$$U_{HOR} = \frac{RT}{2F}\log\left(\frac{P_{H_2}}{P_{H_2}^{ref}}\right) \quad [V]$$

HOR exchange current densities
$$A_{Pt}i_{0,HOR} = 1.0 \times 10^{11} \cdot \exp\left(\frac{20000}{R}\left(\frac{1}{T_{ref}} - \frac{1}{T}\right)\right) \quad [A\,m^{-3}]$$

ORR equilibrium potential
$$U'_{ORR} = U_{ORR}^0 - \frac{RT}{2F}\log(a_W) \quad [V]$$

ORR standard potential
$$U_{ORR}^0 = 1.23 - 0.0009(T - 298.15) \quad [V]$$

ORR exchange current densities
$$A_{Pt}i_{0,ORR}^{ref} = 8.0 \times 10^6 \cdot \exp\left(\frac{38000}{R}\left(\frac{1}{T_{ref}} - \frac{1}{T}\right)\right) \quad [A\,m^{-3}]$$

Oxygen permeability of ionomer : measured with a membrane form
$$\Psi_{O_2} = 5.0 \times 10^{-15} \exp(1.4a_W) \cdot \exp\left(\frac{17000}{R}\left(\frac{1}{T_{ref}} - \frac{1}{T}\right)\right) \quad [mol\,s^{-1}m^{-1}Pa^{-1}]$$

Ionomer water content
$$\lambda = 1.81 \exp(1.89a_W) \quad [-]$$

Proton conductivity of ionomer : measured with a membrane form
$$\kappa_M = 14.9a_W^{1.75} \cdot \exp\left(\frac{12000}{R}\left(\frac{1}{T_{ref}} - \frac{1}{T}\right)\right) \quad [S\,m^{-1}]$$

Effective proton conductivity of ionomer in catalyst layer
$$\kappa_M^{eff} = \frac{\varepsilon_M}{\tau_M}\kappa_M \quad [Sm^{-1}]$$

Water diffusivity of ionomer : measured with a membrane form
$$D_W = (3.76 + 8.82a_W + 53.5a_W^2 - 76.2a_W^3 + 28a_W^4)$$
$$\times 10^{-10} \cdot \exp\left(\frac{20000}{R}\left(\frac{1}{T_{ref}} - \frac{1}{T}\right)\right) \quad [m^2\,s^{-1}]$$

Effective water diffusivity of ionomer in catalyst layer
$$D_{wat}^{eff} = \varepsilon_M D_{wat} \quad [m^2 s^{-1}]$$

Electro − osmotic drag coefficient of ionomer
$$\xi = 1$$

Binary diffusivity coefficient
$$D_{i,j}^{eff} = \frac{\varepsilon_0}{\tau_0}\frac{0.001 \cdot T^{1.75}}{P(\nu_i^{1/3} + \nu_j^{1/3})^2}\sqrt{\frac{1}{M_i} + \frac{1}{M_j}} \quad [m^2\,s^{-1}]$$

Knudsen diffusivity coefficient
$$D_{Kund,i}^{eff} = \frac{\varepsilon_0}{\tau_0}\frac{2r_{kund}}{3}\sqrt{\frac{8RT}{\pi M_i}} \quad [m^2 s^{-1}]$$

c. Convective heat transfer is ignored, only conduction is considered.

d. Regarding gas diffusion, Stefan−Maxwell equations in GDL and Knudsen diffusion in CL are calculated, and other diffusion effects are ignored.

e. Two layered GDL is treated as a one-layer GDL of average physical properties.

2.2. Reaction model

An agglomerate approach is used for the reaction model in the catalyst layer. In this fashion, the oxygen-reduction-reaction (ORR) kinetic equations with ionomer film over a secondary carbon (w/Pt) agglomerate for PEMFCs have been proposed recently [17,18,21–29]. In this formulation, the transfer current density is described as

$$i_{ORR} = 4F\frac{P_{O2}}{P_{O2}^{ref}}\left(\frac{1}{\dfrac{\delta_{ion}}{a_{ion}^{eff}P_{O2}^{ref}\Psi_{O2,ion}} + \dfrac{1}{\theta_{agg}k_{ORR}}}\right) \quad (2)$$

where P_{O2} is the oxygen partial pressure of gas phase in cathode CL, p_{O2}^{ref} is the reference oxygen partial pressure, a_{ion}^{eff} is the effective ionomer film area, δ_{ion} is the ionomer film thickness, $\Psi_{O2,ion}$ is the oxygen permeability of ionomer and k_{ORR} is the reaction rate. Assuming spherical agglomerate particles, the agglomerate effect θ_{agg} is expressed as

$$\theta_{agg} = \frac{3}{\phi^2}(\phi\coth\phi - 1) \quad (3)$$

where ϕ is Thiele modulus,

$$\phi = r_{agg}^{eff}\sqrt{\frac{k_{ORR}}{P_{O2}^{ref}\Psi_{O2,ion}}} \quad (4)$$

and r_{agg}^{eff} is the effective agglomerate radius. The kinetic rate equation for the ORR is given by a Tafel expression,

$$k_{ORR} = \frac{1}{4F}(1 - \theta_{PtOx})A_{Pt}i_{0,ORR}^{ref}\exp\left(-\frac{\alpha_C F}{RT}\eta_{ORR}\right) \quad (5)$$

where A_{pt} is the Pt surface area per unit geometric MEA area. The overpotential, η_{ORR}, is defined as

$$\eta_{ORR} = -\Phi_C + \Phi_{ion} + U_{ORR} \quad (6)$$

Table 3
Physical properties of components for MEA1.

Property	Value sources		aGDL	aCL	Mem	cCL	cGDL	unit
Thickness	measured	δ	2×10^{-4}	3×10^{-6}	3×10^{-5}	5×10^{-6}	2×10^{-4}	m
Porosity	calculated	ε_0	0.75	0.6	−	0.62	0.75	
Tortuosity	fitted	τ_0	3	4	−	4	3	
Electrical conductivity	measured	σ_e	250	60	−	60	250	S m^{-1}
Thermal conductivity	measured	k_q	0.33	0.5	0.26	0.5	0.33	W m^{-1} K^{-1}
Gas permeability	measured	k_G	1.2×10^{-13}	5×10^{-14}	−	5×10^{-14}	1.2×10^{-13}	m^2
Knudsen radius	assumed	r_{kund}	−	4×10^{-8}	−	4×10^{-8}	−	m
Ionomer fraction	calculated	ε_M	−	0.2	−	0.15	−	
Ionomer tortuosity	measured	τ_M	−	1	−	7	−	
Transfer coefficient	assumed	α_a	−	1	−	−	−	
Transfer coefficient	assumed	α_e	−	−	−	0.5	−	
Phase change rate coefficient	assumed	k_{GM}	−	4.0×10^5	−	4.0×10^5	−	s^{-1}
Effective agglomerate radius	fitted	r_{agg}^{eff}	−	−	−	1.2×10^{-7}	−	m
Ionomer film thickness	fitted	δ_{ion}	−	−	−	1×10^{-7}	−	m
Effective ionomer film area	fitted	a_{ion}^{eff}	−	−	−	1.5×10^5	−	m^{-1}

where U_{ORR} is the equilibrium potential and Φ_c and Φ_{ion} are the potential in the carbon and ionomer phases, respectively. In Eq. (5), the effect of platinum oxides (PtO$_x$) is considered in the θ_{PtOx} term, which is the surface coverage ratio by PtO$_x$ as explained below.

In cases of diffusion limited region where the limiting current density (I_{lim}) is observed and k_{ORR} is large enough, Eq. (2) can be written as the following using the ionomer related transport resistance ($R_{CL,ion}$)

$$i_{ORR}|_{k_{ORR}\to\infty} = 4FP_{O2}\left(\frac{a_{ion}^{eff}\cdot\Psi_{O2,ion}}{\delta_{ion}}\right) = \frac{4FP_{O2}}{RTd}\frac{1}{R_{CL,ion}} \qquad (7)$$

$$R_{CL,ion} = \frac{4F}{I_{lim}}\left(\frac{P_{O2}}{RT}\right) = C_{O2,CL}\frac{4F}{I_{lim}} \qquad (8)$$

where d is the thickness of the cathode CL and $C_{O2,CL}$ is the oxygen concentration of gas phase in the cathode CL.

As noted in Eq. (5), we consider the effect of PtO$_x$ coverage. PtO$_x$ forms on the surface of the Pt catalyst above 0.6 V in the presence of water or oxygen. These oxides disturb and inhibit the ORR and subsequently lower the cell voltage. Several forms of oxide and its models are supposed and their impact have been measured [10,30,31]. Here, a simplified model to simulate PtO$_x$ is employed, which assumes a single electrochemical reaction governed by a Butler-Volmer equation,

$$\frac{d\theta_{PtOx}}{dt} = k_{PtOx}\left((1-\theta_{PtOx})\exp\left(\frac{\alpha_a'F}{RT}\eta_{PtOx}\right) - \theta_{PtOx}\exp\left(\frac{-\alpha_c'F}{RT}\eta_{PtOx}\right)\right) \qquad (9)$$

$$\eta_{PtOx} = -\Phi_C + \Phi_{ion} + U_{PtOx} \qquad (10)$$

where k_{PtOx} is the reaction rate for PtOx formation. α_a' and α_c' is the anodic and cathodic transfer coefficient for PtO$_x$ formation, respectively. U_{PtOx} is the PtO$_x$ equilibrium potential. From Eq. (9), the PtO$_x$ coverage ratio under steady-state conditions can be expressed as

$$\theta_{PtOx} = \frac{\exp\left(\frac{\alpha_a'F}{RT}\eta_{PtOx}\right)}{\exp\left(\frac{\alpha_a'F}{RT}\eta_{PtOx}\right)+\exp\left(\frac{-\alpha_c'F}{RT}\eta_{PtOx}\right)} \qquad (11)$$

The calculated relation between θ_{PtOx} and Φ_c - Φ_{ion} is shown in Fig. 2. Using Eq. (11) in Eq. (5), Eq. (5) can be rewritten as (see Appendix A for the detailed derivation)
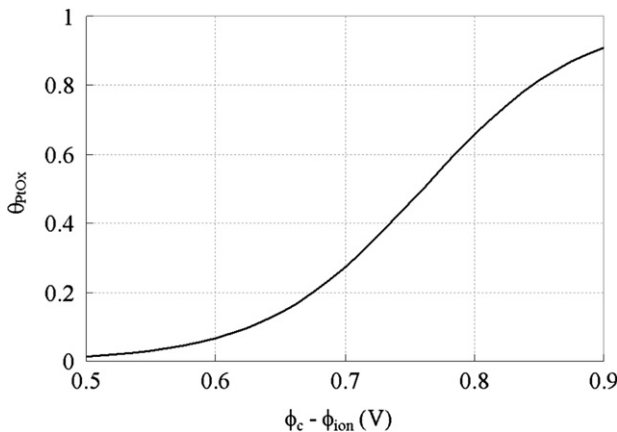

Fig. 2. The relation between Φ_c - Φ_{ion} and PtOx coverage ratio (θ_{PtOx}).

$$\eta_{ORR} \approx \frac{RT}{(\alpha_a'+\alpha_c'+\alpha_C)F}\ln\left(\frac{A_{Pt}i_{0,ORR}^{ref}}{i_{ORR}}\right)$$
$$+ const \quad (\text{Cell voltage}>>0.86V) \qquad (12)$$

Therefore, to keep the Tafel slope nearly 70 mV/decade at 353 K,

$$\alpha_a'+\alpha_c'+\alpha_C = 1 \qquad (13)$$

Hence, we used parameter values of $\alpha_a' = \alpha_c' = 0.25$, $\alpha_c = 0.5$, and $U_{PtOx} = 0.76$ V from literature data [30].

2.3. Polarization-curve fitting

The measured polarization curves are fitted using the following methodology. The fitted parameters as well as other parameters are shown in Table 3.

(1) Most of the physical properties of GDL and membrane are assigned from existing database. For example, we used measured values for electrical conductivity and thermal conductivity of GDL with direct steady state method. The contact heat resistance was included in the bulk value.
(2) Interfacial electric resistance of the cell is fit to 40 mΩcm^{-2} from the measured cell resistance with the current interrupting method.
(3) Ionomer tortuosity is calculated from the proton impedance measurement of CL.
(4) Parameters of the CL such as volume fraction of pore and ionomer are calculated from the thickness of CL, carbon/ionomer ratio, and Pt/carbon ratio.
(5) Tortuosity of GDL is fit to the transport resistance results. Tortuosity of CL is assumed to be small as experimentally reported [16].
(6) $A_{pt}i_{0,ORR} \times d$ is fit to the polarization curves (both initial and cycled) at the low-current-density region (<0.2 A cm^{-2}).
(7) $\delta_{ion}/a_{ion}^{eff} \times d$ is fit to the polarization curves (at initial stage) with 1% oxygen concentration.
(8) Effective agglomerate radius (r_{agg}^{eff}) is obtained by fitting the initial polarization curve with 1% dry-oxygen concentration.

3. Experimental

Electrodes of the Pt/C catalysts were fabricated by a direct-spray method onto the perfluorinated-polymer type membrane. The anode and cathode Pt loadings were 0.05 and 0.1 mg-Ptcm^{-2} (30 wt % Pt/C Tanaka Kikinzoku Kogyo), respectively, and the cathode ionomer/carbon weight ratio (I/C ratio) was 0.75. The same fabrication method was used for other MEAs used in this report with different species, loadings, and Pt/C weight ratios.

The fabricated MEA (MEA1) was placed in a 13 cm^2 (3.6 × 3.6 cm) test cell for the polarization, cyclic-voltammetry (CV), and potential-cycling measurements. For the initial transport-resistance measurement, a 1 cm^2 (1 × 1 cm) test cell was used to ensure high stoichiometry for the diluted oxygen feed. MEAs were sandwiched by GDLs consisting of PTFE treated carbon paper (200 μm thickness) and a microporous layer with an assembly pressure of 1.0 MPa. Porous-metal gas channels (Ti with gold plating) were used in a cross-flow orientation.

MEA1 was tested for initial H$_2$/Air polarization performance and CV and transport-resistance measurements. The cell conditions are summarized in Table 4. Polarization curves were measured under fully humidified conditions with a cathodic sweep rate of 50 mA s^{-1} using a commercial fuel-cell test station (850 series®, Scribner Associates). For the transport-resistance measurements, polarization

Table 4
Cell conditions.

	Atmosphere (flow rate) / NL min^{-1}		Pressure / kPa abs	Temperature / °C	RH / %
	Anode	Cathode			
CV measurement	H$_2$ (2)	Fluorinert™ FC-3283 (−)	100	40	100
Potential cycling	H$_2$ (2)	N$_2$ (2)	100	80	100
Polarization curve measurement	H$_2$ (2)	Air (2)	200	80	90
Transport resistance measurement	H$_2$ (2)	1% O$_2$ 99% N$_2$ or He (2)	150	80	90

curves were measured using 1% O$_2$/99% N$_2$ or He dry gas mole fraction with a cathodic sweep rate of 5 mV s^{-1} using an AS-510-ECA® potentiostat (NF Corporation). Unintentional flooding or membrane dehydration was avoided by monitoring the high-frequency cell-resistance and cell-voltage stability.

CV measurements were performed using an AS-510-ECA® potentiostat (NF Corporation) by sweeping the potential between 0 and 1.0 V vs. RHE at 40, 50, 60 and 80 mV/s sweep rates. While measuring the voltammogram, humidified H$_2$ gas was fed into the anode flow field and the cathode electrode was filled with Fluorinert™ FC-3283 (perfluorohydrocarbon liquid, 3M™) [32]. If N$_2$ gas is fed into cathode flow field, then hydrogen evolution would contribute significantly to the total current measured at the low-potential region (<0.2 V) of the hydrogen-adsorption curves, and this effect could lead to the overestimation of the ECSA [33]. By adopting the above method instead of using N$_2$ gas, it is possible to make the hydrogen-evolution potential lower and mitigate such error. The ECSA was determined from the total charge for hydrogen adsorption by integrating between a straight baseline drawn from the double-layer-capacitance region (0.4 V) and the final minimum potential (0 V) in the cathodic CV spectrum. The total charge for hydrogen adsorption depends on the sweep rate and the effect of hydrogen evolution on the total charge decreased as the sweep rate increased (Fig. 3). Therefore, extrapolation to infinite sweep rate was used to determine the charge; this method can minimize the effect of hydrogen evolution [33]. Then, 210 μC cm^{-2}-Pt capacitance was used to determine the ECSA.

Finally, MEA-voltage-cycling experiments were conducted up to 49000 cycles using a square-wave potential from 0.7 V to 0.9 V vs RHE for 4 s each under fully humidified conditions with H$_2$/N$_2$ (see Table 4 for other conditions). During the cycles, CV spectra and polarization curves were measured after 5000, 13000, 28000, 39000 and 49000 cycles.
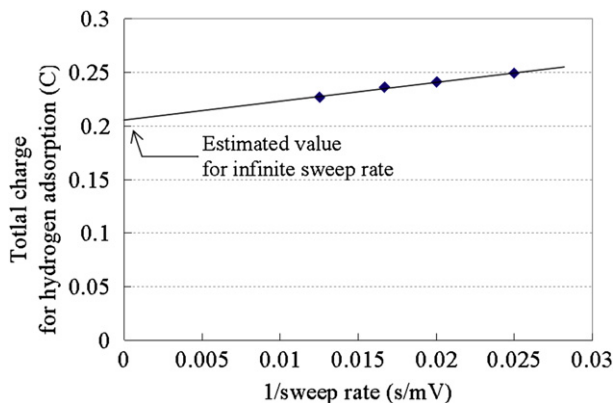
4. Results and discussion

4.1. Transport resistance in the catalyst layer

The initial polarization performance is shown in Fig. 4. The tests used 1% O$_2$ in N$_2$ or He balance gas and the limiting current density was 0.22 Acm^{-2} and 0.32 Acm^{-2} for the N$_2$ and He cases, respectively. The total transport resistance in the cathode (R_{tot}) was then calculated from the limiting current and the oxygen concentration in cathode flow field using

$$R_{tot} = C_{O2,GC}4F/I_{lim} = R_{CL,tot} + R_{GDL} \qquad (14)$$

where $C_{O2,GC}$ is the oxygen concentration of gas phase in cathode flow field. To distinguish the transport resistance in CL ($R_{CL,tot}$) from the transport resistance in GDL (R_{GDL}), the difference of molecular diffusivities is used for the two balance gases ($D_{O2\ in\ He}/D_{O2\ in\ N2} = 2.19$ at 80 °C and 150 kPa). As the average pore size of GDL is 10−100 μm, most diffusion through the GDL occurs by molecular diffusion. On the other hand, $R_{CL,tot}$ consists of Knudsen diffusion (pore size of 0.01−0.1 μm) and permeation resistances through the ionomer film, which are independent of the balance gas. Using the above relations, $R_{CL,tot}$ was calculated as 28 s m^{-1} and R_{GDL} was calculated as 37 s m^{-1} and 17 s m^{-1} for the N$_2$ and He conditions, respectively.

From the initial ECSA measurement, the area was calculated to be 71 m^2 m^{-2} at the initial stage. Because this value almost agrees with the total Pt surface area (A_{Pt}) estimated from the average Pt radius of 4.1 nm obtained from XRD measurement, the whole Pt surface on MEA1 is considered to be electrochemically active. Fig. 5(a) shows the measured ECSA during the potential cycling for MEA1, and it is found that the ECSA decreased to 27 m^2 m^{-2} at the end of the potential cycling test. In terms of polarization, Fig. 5(b) shows the measured curves at each stage including both the data and the model-fit lines. From the curves, the performance decayed over the entire region. The measured potential difference at 1.7 Acm^{-2} at the end of the test was 170 mV which is more than 5 times larger than that at 0.2 Acm^{-2}. In the experiments, the large performance decay at high current density (>1 Acm^{-2}) was observed as well as the small performance decay at kinetic region. The simulated polarization curves described the same tendency. The performance decay both at 0.2 and 1.7 Acm^{-2} are shown in Fig. 5(c). The performance decline slope of 1.7 Acm^{-2} is significantly steeper than that of 0.2 Acm^{-2}, which is well reproduced by the simulation.

The oxygen transport resistance in a typical PEMFC consists of molecular diffusion resistance in GDL, Knudsen diffusion resistance in the gas phase of the catalyst layer ($R_{CL,gas}$), and permeation
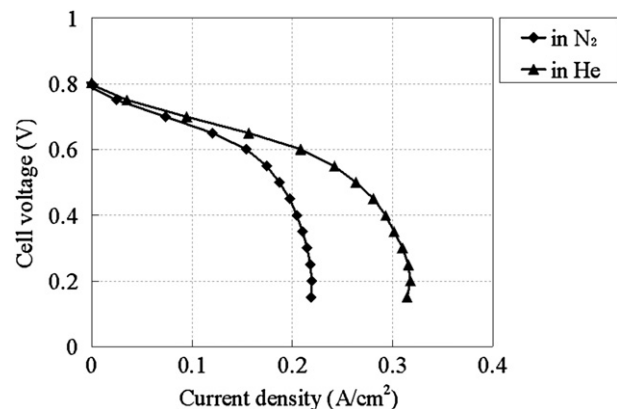

Fig. 3. Total charge for hydrogen adsorption as a function of potential sweep rate with different sweep rates of 40, 50, 60 and 80 mV/s for MEA1 at initial stage.

Fig. 4. Polarization curves of limiting current measurement of MEA1 at initial stage in 1% O$_2$ (dry) with balance gases of N$_2$ or He, at 80 °C, 150 kPa and 90% relative humidity.
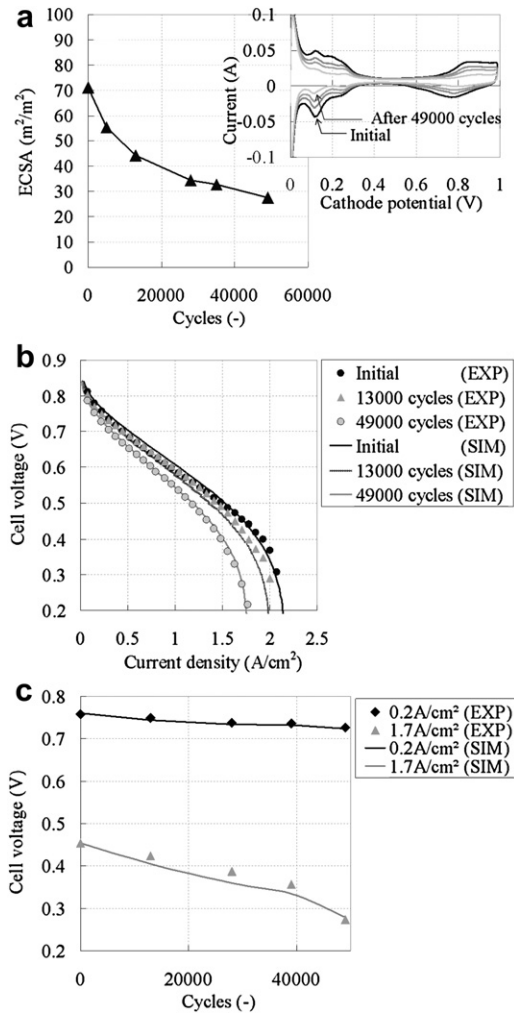
Fig. 5. (a) Measured ECSA with 50 mV/s (inset of (a)) CV spectra. (b) Measured polarization curves of MEA1 during the potential cycling and model-fit lines. (c) Cell voltage with respect to cycles at 0.2 and 1.7 Acm^{-2}.

resistance through the ionomer film surrounding the catalyst layer agglomerates ($R_{CL,ion}$) [16]. The total transport resistance ($R_{CL,tot}$) in the CL can be written as

$$R_{CL,tot} = R_{CL,ion} + R_{CL,gas} \tag{15}$$

The schematic illustration of the effective ionomer film area (a_{ion}^{eff}) and the Pt surface area (A_{Pt}) is shown in Fig. 6(a). a_{ion}^{eff} is the ionomer film area surrounding a Pt particle that is effectively used for oxygen permeation. One can assume that a_{ion}^{eff} is roughly proportional to A_{Pt}

$$a_{ion}^{eff} \propto A_{Pt} \tag{16}$$

Accordingly, using Eq. (16) in Eq. (7), $R_{CL,ion}$ is expressed as

$$R_{CL,ion} \propto 1/A_{Pt} \tag{17}$$

Combining Eq. (15) with Eq. (17), $R_{CL,tot}$ is rewritten as

$$R_{CL,tot} = \frac{C_1}{A_{Pt}} + C_2 = \frac{C_1}{ECSA} + C_2 \tag{18}$$

where C_1 and C_2 are constants. This relationship indicates $R_{CL,tot}$ is inverse proportional to ECSA, provided the ionomer film thickness is fixed. On the other hand, the experimental results of the relation
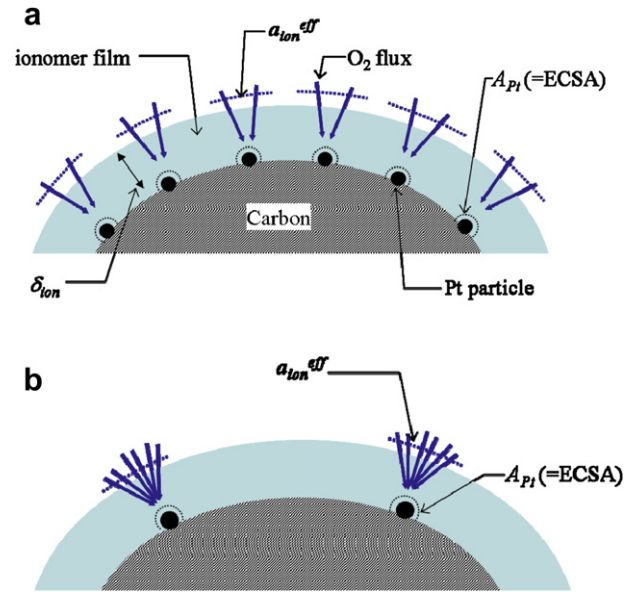

Fig. 6. Schematic illustration of Pt surface area (A_{Pt}), effective ionomer area (a_{ion}^{eff}), and ionomer film thickness (δ_{ion}) in catalyst layer. (a) At initial stage. (b) After degradation.

between ECSA and $R_{CL,tot}$ for MEA1 are shown in Fig. 7. The other experimental results of various MEAs with different Pt species, loadings and Pt/C weight ratios are also shown in the same figure. The dotted line is the fitting curve using Eq. (18) ($C_1 = 1700$ s m^{-1} and $C_2 = 5$ s m^{-1}), which shows good agreement, thereby indicating the assumption of Eq. (16) is rational.

$R_{CL,tot}$ can be calculated using Eq. (18) from the measured ECSA during the potential cycling. The calculated $R_{CL,tot}$ and ratio of a_{ion}^{eff} change are shown in Fig. 8. $R_{CL,tot}$ increased from 28 s m^{-1} at initial stage to 67 s m^{-1} as a_{ion}^{eff} decreased by 62%. The explanation of increased $R_{CL,tot}$ after potential cycling can be explained as in Fig. 6(b). Pt particles in the cathode catalyst layer dissolve at high potential and either diffuse into the membrane or merge onto larger Pt particles (Ostwald-ripening), resulting in the total ECSA decrease. Therefore, the mechanism of this increase of $R_{CL,tot}$ is similar to that of the case of low Pt loading [15–17], that is to say, a higher flux through the ionomer film is needed to maintain the same total current density after ECSA decreases. Thus, the oxygen-concentration slope within the ionomer film becomes steep, resulting in lower oxygen concentrations at the surface of Pt particles (see Eq. (2)).
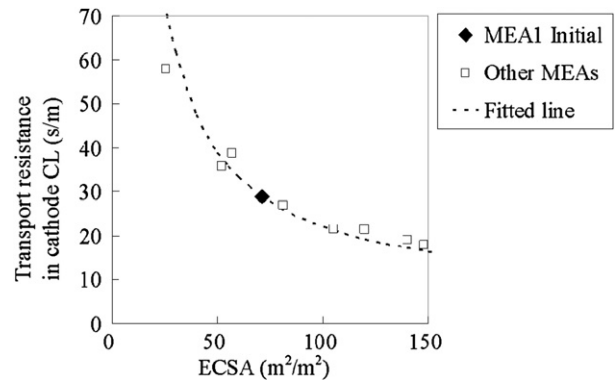

Fig. 7. The relation between ECSA and the transport resistance in cathode CL at the initial stage of MEA1 (◆), MEAs with different Pt species, loadings and Pt/C weight ratios (□), and the fitted line of Eq. (18) (–). All data are measured at 80 °C, 150 kPa and 90% relative humidity.
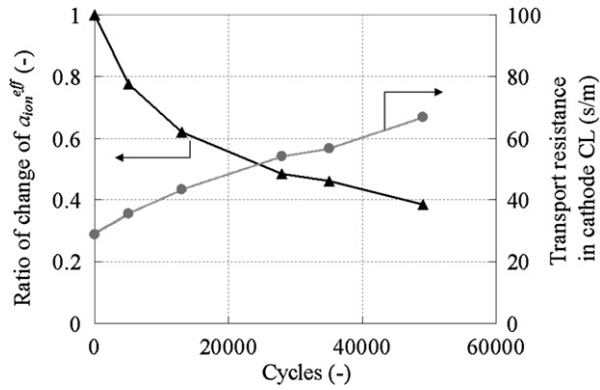
Fig. 8. The calculated ratio of change of a_{ion}^{eff} (▲) and the transport resistance in cathode CL ($R_{CL,tot}$) (●) of MEA1 using Eq. (18) at 80 °C, 150 kPa and 90% relative humidity.

4.2. Understanding losses

As the performance decay strongly depends on current density, the breakdown of the increased overpotential during the potential cycling was studied. The total increased overpotential in the cathode CL (= total performance decay) is classified into three sources: activity and oxygen and proton transport. The activity overpotential is mainly caused by the ORR activity decrease; therefore the performance decay only with the activity-overpotential effect is calculated by reducing A_{Pt} based on Eq. (5); here Fig. 5(a) is used for the changing ratio of A_{Pt}. The increase in the oxygen transport overpotential is caused by the increased oxygen-transport resistance in the cathode CL as written in Eqs. (7) and (8). Therefore, the increased transport overpotential is expressed by the gap between the following two calculation results. One is the calculation result of reducing only A_{Pt} and the other is the calculation result of reducing both A_{Pt} and a_{ion}^{eff} using the relation of Eq. (18). The increase in the proton-transport over-potential is caused by changing the proton-transport distance in the ionomer by shifting the reaction distribution across the cathode CL. The proton-transport resistance overpotential ($\eta_{H,CL}$) is esti-mated by the ionomer potential drop from the membrane boundary to the average reaction center in the cathode CL

$$\eta_{H,CL} = \Phi_{ion} + U_{ORR} - \Phi_C - \frac{\int_0^1 i_{ORR}(z)\eta_{ORR}(z)\mathrm{d}z}{\int_0^1 i_{ORR}(z)\mathrm{d}z} \quad (19)$$

where z is the cross-sectional MEA dimension from the membrane.

The polarization curve after 49000 cycles was analyzed using the above method. The three curves (shown in Fig. 9(a)) were calculated: initial stage [A], only increase in the activity over-potential [B], and increases in both the activity and transport overpotentials [C]. The figure indicates that most of the perfor-mance decay less than 1.0 Acm^{-2} is caused by the increase in the activity overpotential, while over 1 Acm^{-2} the transport over-potential increase is dominant (see Fig. 9(b)). At 1.7 Acm^{-2} the transport overpotential increase was more than 100 mV compared to 5 mV at 0.2 Acm^{-2}. The effect of the increase in the activity overpotential was about 40 mV and slightly increased at 1.7 Acm^{-2}. The increase in the proton overpotential was negligible even at high current densities due to fully humidified inlets (i.e., the reaction
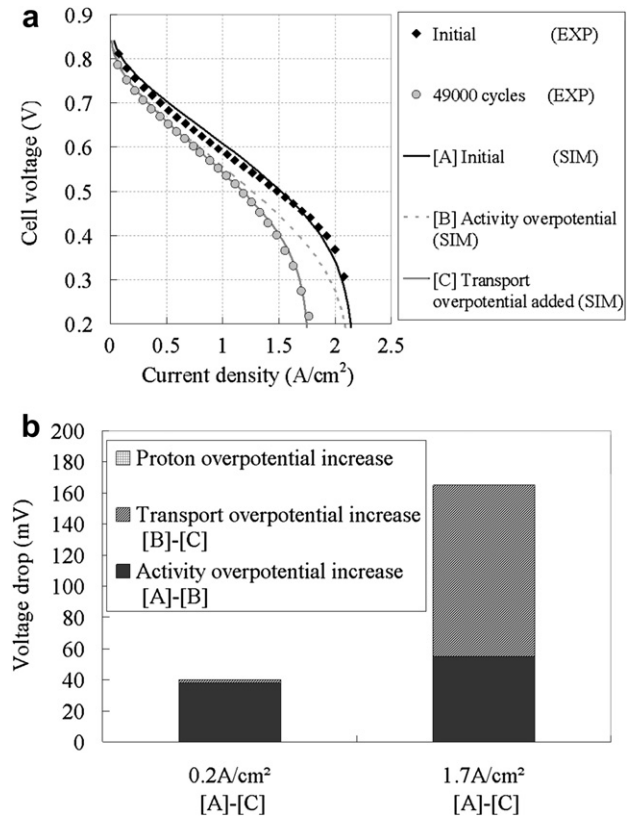

Fig. 9. (a) The influence of each overpotential on the polarization curve after 49000 cycles. Dots are the experimental results and calculated lines are overlaid. Lines are initial [A], only with activity overpotential increase considered [B], and with transport overpotential increase added [C]. (b) The breakdown of the performance decay at 0.2 and 1.7 Acm^{-2} after 49000 cycles.

distribution within the cathode CL did not change after degradation).

4.2.1. Limiting case 1: low-humidity condition

At low-humidity conditions, however, the proton overpotential can become significant. To study this effect, simulations were conducted using the same parameters as those used for MEA1. Here we calculated 3 cases under low-humidity conditions. The first case is the initial stage [D], the second is after degradation (49000 cycles) with uniform ECSA decrease [E], and the third is after degradation with nonuniform ECSA distribution [F] (Fig. 10(a) inset). The ECSA distribution across the cathode CL becomes nonuniform after potential cycling where there is less ECSA remaining near the membrane side of the CL [1,9,12]. Polarization curves were then calculated for each case (Fig. 10(a)). The large performance decay is observed in case [E] and [F], and the analysis of the breakdown of the overpotential increase was conducted using the same methodology as discussed above. Fig. 11(b) is the analysis results at 1 Acm^{-2} at each case with different humidity conditions. In addition to the transport over-potential increase, there are some additional increases in the proton overpotential.

The increased proton overpotential is explained by the change of the reaction distribution across the CL after degradation. In general, under low-humidity conditions, more reaction occurs near the membrane side of the CL because the ionomer proton-transport resistance is significant. However, in case [E], the reaction distri-bution is unable to move toward the membrane side because of the resultant higher oxygen-transport resistance. In other words, the
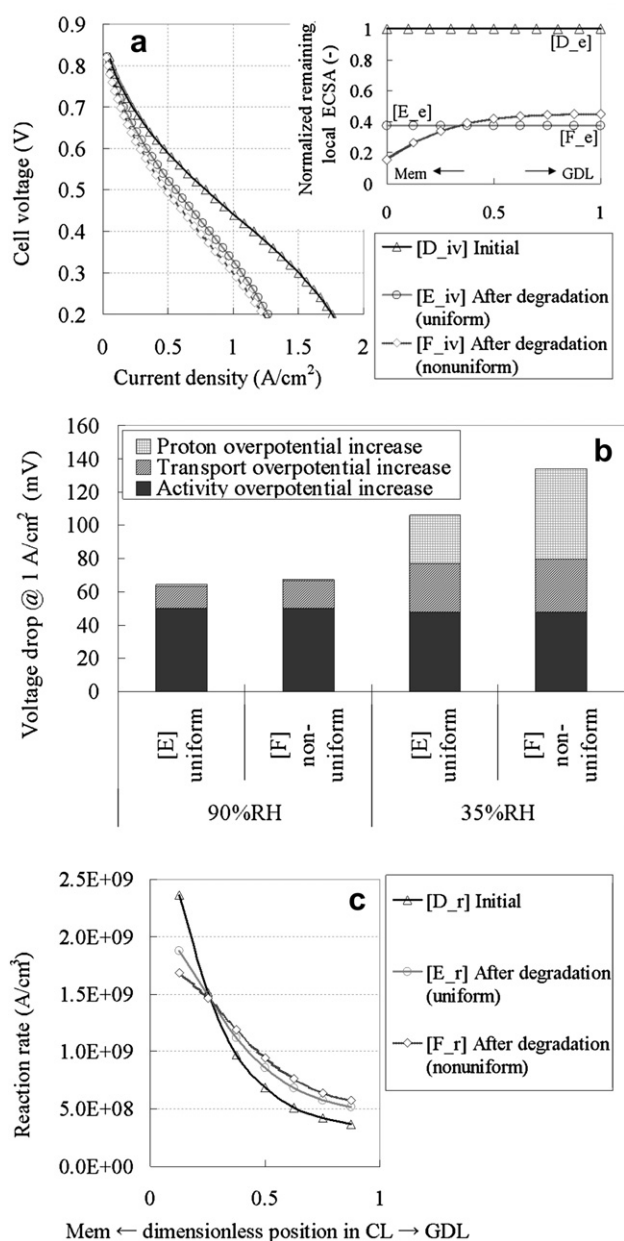
Fig. 10. (a) Calculated polarization curves of MEA1 with 35% relative humidity for each case of [D_e], [E_e] and [F_e]. (inset of (a)) assumed normalized local ECSA across the CL for MEA1 at initial stage [D_e], after 49000 cycles with uniform ECSA decrease [E_e], and after 49000 cycles with nonuniform ECSA decrease [F_e]. (b) Breakdown of the cause of the performance decay at 1 Acm^{-2} at each case for different humidity conditions. (c) Calculated reaction rate distributions across cathode CL at 1 Acm^{-2} with 35% RH for each case of [D_e], [E_e] and [F_e].

current distribution becomes more uniform across the CL (Fig. 10(c) [E_r]) in order to minimize the total potential loss comprised of both the proton- and oxygen transport overpotentials. This current-distribution change is amplified in case [F], where there is less ECSA remaining near the membrane side (Fig. 10(c)[F_r]). In this case, the additional proton overpotential occurs because the proton-transport distance becomes even longer.

4.2.2. Limiting case 2: low-oxygen-concentration condition

In practical vehicle use, it is efficient to set the gas stoichiometry as low as possible. With a typical air stoichiometry of about 1.4, the dry oxygen concentration at the cell outlet becomes 7%, so
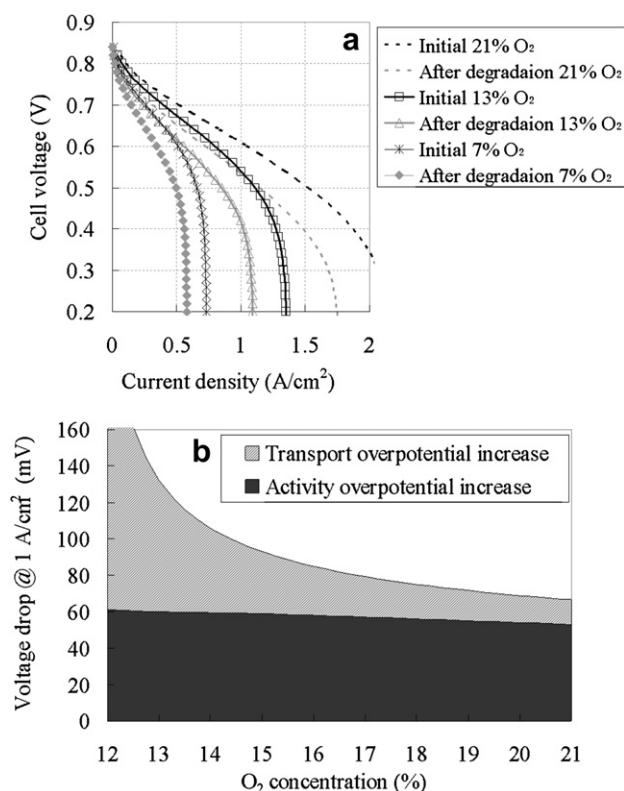

Fig. 11. (a) Calculated polarization curves at initial stage and after degradation with different oxygen concentration under 90% relative humidity at 80 °C and 150 kPa. (b) The relation between increased overpotential at 1.0 Acm^{-2} and dry oxygen concentration in the cathode flow field.

the average oxygen concentration is about 14%. Generally, the transport overpotential becomes larger as the current density approaches the limiting current density because the oxygen concentration at the Pt surface approaches zero. It is important to note that the limiting current depends on humidity as well. For example, the oxygen partial pressure is nearly 30% larger at 30% relative humidity compared with 100% relative humidity with 150 kPa total pressure at 80 °C. Fig. 11(a) shows the calculated polarization curves with different oxygen concentrations at 90% relative humidity at 80 °C. Performance decay at the high-current-density range is significant with low oxygen concentration. Fig. 11(b) is the relation between the average dry oxygen concentration in the cathode flow field and the overpotential increase after degradation at 1 cm^{-2}. It is evident that the transport overpotential increase becomes significant as oxygen concentration becomes lower while the activity overpotential increase after degradation is almost identical and independent of the oxygen concentration.

5. Conclusions

The relation between physical property change and performance decay after degradation has been analyzed using a detailed PEMFC 1D model. In the model, the effective ionomer film area (a_{ion}^{eff}), which describes the total surface area of ionomer used for effective oxygen permeation, is used to express the oxygen transport in the catalyst layer (CL). The analysis of polarization curves after potential cycling demonstrated the important correlation of $a_{ion}^{eff} \propto A_{pt}$ It is concluded that the large performance decay at high current density is mostly explained by the increased transport

resistance in the cathode CL. Therefore, the measurement of ECSA during degradation is important to estimate not only the increase in activity overpotential due to surface area loss, but also the increase in the transport overpotential. The remaining small deviation between simulation and experiments may be explained by such factors as catalyst-layer structural changes, ionomer degradation (physical property changes), and carbon corrosion. For the case of low-humidity operation, simulation results show that the performance decay expanded after degradation compared with the high-humidity condition. This effect is because the reaction current distribution shifts away from the membrane interface due to the oxygen-transport-resistance increase in the cathode CL, which is compounded by the nonuniform ECSA distribution across the CL. By taking a_{ion}^{eff} into account in the model, the performance decay can be estimated accurately.

Acknowledgments

Appendix A

Eq. (12) can be derived as follows. Eq. (5) can be written as

$$\eta_{ORR} = \frac{RT}{\alpha_C F}\left[\ln\left(\frac{A_{Pt}i_{0,ORR}^{ref}}{i_{ORR}}\right) + \ln(1 - \theta_{PtOx})\right] \quad (A\text{-}1)$$

Substituting Eq. (11) into Eq. (A-1), η_{ORR} is expressed as

$$\eta_{ORR} = \frac{RT}{\alpha_C F}\left[\ln\left(\frac{A_{Pt}i_{0,ORR}^{ref}}{i_{ORR}}\right) \right.$$
$$\left. + \ln\left(\frac{\exp\left(\frac{-\alpha_c' F}{RT}\eta_{PtOx}\right)}{\exp\left(\frac{\alpha_a' F}{RT}\eta_{PtO}\right) + \exp\left(\frac{-\alpha_c' F}{RT}\eta_{PtOx}\right)}\right)\right] \quad (A\text{-}2)$$

For the case of cell voltage higher than 0.86 V, where the cathodic reaction is negligible compared to the anodic reaction, η_{ORR} is

$$\eta_{ORR} \approx \frac{RT}{\alpha_C F}\left[\ln\left(\frac{A_{Pt}i_{0,ORR}^{ref}}{i_{ORR}}\right) \right.$$
$$\left. + \ln\left(\frac{\exp\left(\frac{-\alpha_c' F}{RT}\eta_{PtOx}\right)}{\exp\left(\frac{\alpha_a' F}{RT}\eta_{PtOx}\right)}\right)\right] \quad (Cell\ voltage > 0.86V) \quad (A-3)$$

By using the relation of Eq. (10) into Eq. (A-3) with the value of $U_{ORR} = 1.18$ V and $U_{PtOx} = 0.76$ V, η_{ORR} is

$$\eta_{ORR} = \frac{RT}{\alpha_C F}\ln\left(\frac{A_{Pt}i_{0,ORR}^{ref}}{i_{ORR}}\right) - \frac{(\alpha_a' + \alpha_c')}{\alpha_C}(\eta_{ORR} + 0.42) \quad (A\text{-}4)$$

Finally, η_{ORR} is expressed as

$$\eta_{ORR} \approx \frac{RT}{(\alpha_a' + \alpha_c' + \alpha_C)F}\ln\left(\frac{A_{Pt}i_{0,ORR}^{ref}}{i_{ORR}}\right) + const \quad (A\text{-}5)$$

Nomenclature

A_P	Pt surface area per unit area of MEA, m^2 m^{-2}
a_w	Water activity, $-$
a_{ion}^{eff}	Effective surface area of ionomer film on catalyst per unit volume of CL, m^2 m^{-3}
C	Molar concentration, mol m^{-3}
d	Catalyst layer thickness, m
$D_{i,j}$	Binary diffusion coefficient of i and j, m^2 s^{-1}
D_{knud}	Knudsen diffusion coefficient, m^2 s^{-1}
D_w	Diffusion coefficient of water, m^2 s^{-1}
ECSA	Electrochemical surface area per unit area of MEA, m^2 m^{-2}
F	Faraday constant, 96485 C mol^{-1}
i_0	Exchange current density, A m^{-3}
i	Current density per unit volume, A m^{-3}
I_{lim}	Limiting current density, A m^{-2}
J	Flow rate, mol s^{-1}
J_{GM}	Evaporation/condensation rate between gas and ionomer phase, mol m^{-3} s^{-1}
k_{GM}	Evaporation/condensation coefficient between gas and ionomer phase, s^{-1}
k_G	Gas permeability, m^2
k_{ORR}	Reaction rate, mol m^{-3} s^{-1}
k_{PtOx}	Reaction rate for platinum oxidation, mol m^{-3} s^{-1}
k_q	Thermal conductivity, W m^{-1} K^{-1}
M	Molecular weight, $-$
N	Flux, mol m^{-2} s^{-1}
P_i	Partial pressure, Pa
P	Total pressure, Pa
Q	Heat generation, J m^{-3}
r_{knud}	Knudsen diffusion radius, m
r_{agg}^{eff}	Effective agglomerate radius, m
R	Gas constant, J mol^{-1} K^{-1}
R_i	Transport resistance, s m^{-1}
R_{tot}	Total transport resistance in CL, s m^{-1}
T	Absolute temperature, K
U	Equilibrium potential, V
v_G	Gas velocity, m s^{-1}
z	Distribution domain for cross-sectional direction of MEA, $-$

Greek

α_a	Anodic transfer coefficient
α_c	Cathode transfer coefficient
α_a'	Anodic transfer coefficient for platinum oxidation
α_c'	Cathode transfer coefficient for platinum oxidation
δ_{ion}	Ionomer film thickness, m
η	Activation overpotential, V
ε	Fraction, $-$
θ	Pt utilization (agglomerate), $-$
θ_{PtOx}	PtOx coverage ratio, $-$
κ	Proton conductivity, S m^{-1}
λ	Water content, mol mol^{-1}
μ	Viscosity, Pa s
μ_w	Chemical potential of water in membrane, J mol^{-1}
ξ	Electro-osmotic drag coefficient, $-$
ρ	Bulk density, kg mol^{-1} $-$
σ_e	Electric conductivity, S m^{-1}
τ	Tortuosity, $-$
ϕ	Theile modulus, $-$
Φ	Potential, V
$\Psi_{O2,ion}$	Oxygen permeability of ionomer, mol s^{-1} m^{-2} Pa^{-1}

Subscripts and superscripts

CL	Catalyst layer
eff	Effective value

gas	Gas phase
GC	Gas channel
GDL	Gas diffusion layer
HOR	Hydrogen oxidation reaction
i	generic species
ion	Ionomer phase
j	generic species
M	Membrane phase
ORR	Oxygen reduction reaction
PtOx	Platinum oxides
ref	Reference value
vap	vapor phase
wat	water phase
0	gas phase

References

[1] P.J. Ferreira, G.J. la O', Y.S. Horn, D. Morgan, R. Makharia, S. Kocha, et al., J Electrochem Soc 152 (11) (2005) A2256−A2271.

[2] F.T. Wagner, H.A. Gasteiger, R. Makharia, K.C. Neyerlin, E.L. Thompson, S.G. Yan, ECS Trans 3 (1) (2006) 19−29.

[3] R. Makharia, S.S. Kocha, P.T. Yu, M.A. Sweikart, W. Gu, F.T. Wagner, et al., ECS Trans 1 (8) (2006) 3−18.

[4] C. Grolleau, C. Coutanceau, F. Pierre, J.M. Leger, Electrochim Acta 53 (2008) 7157−7165.

[5] L. Dubau, F. Maillard, M. Chatenet, J. Andre, E. Rossinot, ECS Trans 33 (1) (2010) 407−417.

[6] R.M. Darling, J.P. Meyers, J Electrochem Soc 150 (11) (2003) A1523−A1527.

[7] A.V. Virkar, Y. Zhou, J Electrochem Soc 154 (6) (2007) B540−B547.

[8] W. Bi, T.F. Fuller, J Power Sources 178 (2008) 188−196.

[9] M. Mench, E.C. Kumbur, T.N. Veziroglu (Eds.), in: Polymer Electrolyte fuel cell degradation, Academic Press, 2011 (chapter 9).

[10] M. Uchimura, S.S. Kocha, ECS Trans 11 (1) (2007) 1215−1226.

[11] R. Lin, B. Li, Y.P. Hou, J.M. Ma, Int J Hydrogen Energy 34 (2009) 2369−2376.

[12] G.J.M. Janssen, E.F. Sitters, A. Pfrang, J Power Sources 191 (2009) 501−509.

[13] S. Chen, H.A. Gasteiger, K. Hayakawa, T. Tada, Y.S. Horn, J Electrochem Soc 157 (1) (2010) A82−A97.

[14] S. Sugawara, T. Maruyama, Y. Nagahara, S.S. Kocha, K. Shinohara, K. Tsujita, et al., J Power Sources 187 (2009) 324−331.

[15] S. Okazaki, N. Nonoyama, Y. Ikogi, and Y. Yoshida, 50st Battery symposium abst. (2009) 2E20.

[16] N. Nonoyama, S. Okazaki, A.Z. Weber, Y. Ikogi, Y. Yoshida, J Electrochem Soc 158 (4) (2011) B416−B423.

[17] W. Yoon, A.Z. Weber, J Electrochem Soc 158 (8) (2011) B1007−B1018.

[18] Y. Tabe, M. Nishino, H. Takamatsu, T. Chikahisa, J Electrochem Soc 158 (10) (2011) B1246−B1254.

[19] N. Nonoyama, Y. Ikogi, ECS Trans 16 (2) (2008) 13−21.

[20] Process Systems Enterprise Limited: http://www.psenterprise.com/.

[21] A.Z. Weber, J. Newman, J Electrochem Soc 151 (2004) A311−A325.

[22] A.Z. Weber, J. Newman, J Electrochem Soc 151 (2004) A326−A339.

[23] M.L. Perry, J. Newman, E.J. Cairns, J Electrochem Soc 145 (1998) 5−15.

[24] A.Z. Weber, J. Newman, Chem Rev 104 (2004) 4679−4726.

[25] G. Lin, W.S. He, T.V. Nguyen, J Electrochem Soc 151 (2004) A1999−A2006.

[26] D. Harvey, J.G. Pharoah, K. Karan, J Power Sources 179 (2008) 209−219.

[27] K.M. Yin, J Electrochem Soc 152 (2005) A583−A593.

[28] A.A. Shah, G.S. Kim, W. Gervais, A. Young, K. Promislow, J. Li, et al., J Power Sources 160 (2006) 1251−1258.

[29] P.K. Das, X. Li, Z.S. Liu, J Power Sources 179 (2008) 186−199.

[30] Y. Liu, M. Mathias, J. Zhang, Electrochem Solid-State Lett 13 (2010) B1−B3.

[31] J.X. Wang, J. Zhang, R.R. Adzic, J Phys Chem A 111 (2007) 12702−12710.

[32] K. Ikeda, N. Nonoyama, and Y. Ikogi, 51st Battery symposium abst. (2010) 2F22.

[33] R.N. Carter, S.S. Kocha, F.T. Wagner, M. Fay, H.A. Gasteiger, ECS Trans 11 (1) (2007) 403−410.